J. Fluid Mech. (2007), *vol.* 585, *pp.* 323–342.
doi:10.1017/S0022112007006866 Printed in the United Kingdom

Coriolis effects on the elliptical instability in cylindrical and spherical rotating containers

M. LE BARS, S. LE DIZÈS AND P. LE GAL

Institut de Recherche sur les Phénomènes Hors Équilibre – CNRS, Aix-Marseille Université, UMR 6594, 49, rue F. Joliot Curie, B.P. 146, F-13384 Marseille Cedex 13, France

(Received 21 September 2006 and in revised form 11 April 2007)

The effects of the Coriolis force on the elliptical instability are studied experimentally in cylindrical and spherical rotating containers placed on a table rotating at a fixed rate $\tilde{\Omega}^G$. For a given set-up, changing the ratio Ω^G of global rotation $\tilde{\Omega}^G$ to flow rotation $\tilde{\Omega}^F$ leads to the selection of various unstable modes due to the presence of resonance bands, in close agreement with the normal-mode theory. No instability occurs when Ω^G varies between $-3/2$ and $-1/2$ typically. On decreasing Ω^G toward $-1/2$, resonance bands are first discretized for $\Omega^G > 0$ and progressively overlap for $-1/2 < \Omega^G < 0$. Simultaneously, the growth rates and wavenumbers of the prevalent stationary unstable mode significantly increase, in quantitative agreement with the viscous short-wavelength analysis. New complex resonances have been observed for the first time for the sphere, in addition to the standard spin-over. We argue that these results have significant implications in geo- and astrophysical contexts.

1. Introduction

The elliptical instability corresponds to the three-dimensional destabilization of two-dimensional rotating flows with elliptical streamlines. It was first discovered in the context of strained vortices (Moore & Saffman 1975; Tsai & Widnall 1976), but it generally appears in any turbulent flow exhibiting coherent structures with elliptical motion (Pierrehumbert 1986; Bayly 1986). The elliptical instability also occurs in a large range of industrial and natural systems, where the ellipticity is generated either by vortex interactions or by tidal effects. It is for instance expected in the wake vortices behind aircrafts (e.g. Leweke & Williamson 1998), in the intense vortical structures of the atmosphere and the ocean (e.g. Afanasyev 2002), in planetary liquid cores (e.g. Aldridge *et al.* 1997; Kerswell & Malkus 1998; Lacaze *et al.* 2006), or in binary stars and accretion disks (e.g. Lubow, Pringle & Kerswell 1993; Rieutord 2003; Lebovitz & Zweibel 2004). Since its discovery in the mid-1970s, the elliptical instability has thus received considerable attention, theoretically, experimentally and numerically (see for instance the review by Kerswell 2002).

In most practical cases, the strain field responsible for the elliptical pattern rotates around the same axis as the flow, but with a different rate and possibly in the opposite direction. One can thus ask how this global rotation influences the development of the elliptical instability through the induced Coriolis force. Various theoretical studies have been performed, using either a short-wavelength analysis (Craik 1989; Leblanc & Cambon 1997; Le Dizès 2000) or a normal-mode analysis (Gledzer & Ponomarev 1992; Kerswell 1994). They all tend to demonstrate that the global rotation has a stabilizing effect on cyclones and a destabilizing effect on anticyclones, except when the global rotation almost compensates for the flow rotation, in which case

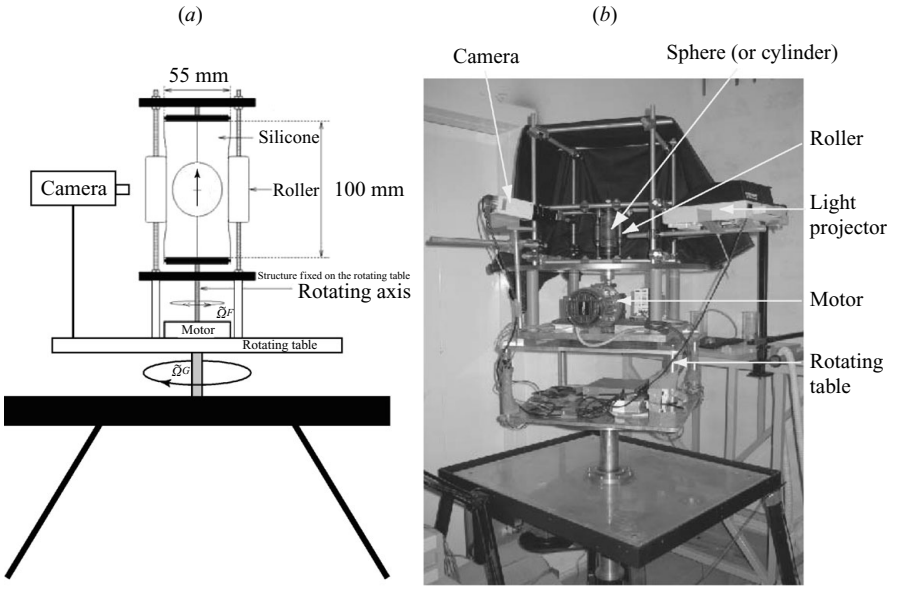

FIGURE 1. (*a*) Sketch and (*b*) photo of the experimental set-up, with the deformed container (either a sphere or a cylinder) placed on the rotating table.

the elliptical instability disappears. This has been confirmed by numerical studies for specific vortices, such as Stuart vortices (Leblanc & Cambon 1998; Potylitsin & Peltier 1999) and Taylor–Green vortices (Sipp, Lauga & Jacquin 1999). From an experimental point of view, Boubnov (1978) first studied the stability of rotating flows in an ellipsoid filled with water, which was sharply stopped after solid-body rotation was reached; the whole set-up was placed on a table rotating at a fixed velocity. He observed both the stabilizing effect of the Coriolis force on rotation around the middle axis of the ellipsoid and the destabilizing effect of the Coriolis force on rotation around the minor and major axes. Using the same method, Vladimirov, Tarasov & Ribok (1983) observed the stabilization of the elliptical instability by the cyclonic Coriolis force in a rigid cylinder of elliptical cross-section. Afanasyev (2002)† generated vortex pairs on a rotating table and observed the selective destabilization of the elliptical anticyclones, with an increasing wavelength when the global rotation goes to zero. Stegner, Pichon & Beunier (2005) noticed the same behaviour in the anticyclonic columns of rotating Bénard–von Kármán vortex streets, provided the ratio Ω^G between the global angular velocity $\tilde{\Omega}^G$ and the flow angular velocity $\tilde{\Omega}^F$ is greater than -1. In all these experiments however, the elliptical instability was observed during a limited time and competed with centrifugal instabilities. No systematic conclusions could thus be derived from these interesting trends.

In the present paper, we focus on the elliptical instability and systematically study the effects of the Coriolis force, both in a rotating cylinder and in a rotating spheroid. Our experimental set-up is inspired by Malkus (1989): it is similar to the one used in Eloy, Le Gal & Le Dizès (2003) and Lacaze, Le Gal & Le Dizès (2004). Unlike previous devices, it permits analysis of growth and saturation of the elliptical instability. As shown in figure 1, a deformable and transparent container – either a cylinder of radius

† See also the study by J. Wells, http://www.physics.mun.ca/∼wellsj/stability.html

$\tilde{R} = 2.75\,\text{cm}$ and height $\tilde{H} = 21.4\,\text{cm}$ or a hollow sphere of radius $\tilde{R} = 2.175\,\text{cm}$ – is set in motion about its axis (Oz) with an angular velocity $\tilde{\Omega}^F$ up to 300 r.p.m. and is simultaneously deformed elliptically by two fixed rollers parallel to (Oz). The container is filled with water seeded with anisotropic particles (kalliroscope). A light sheet is formed in a plane containing the rotation axis for visualization, allowing the measurement of wavelengths and frequencies of excited modes. In the present study, the whole set-up (including camera and light projector) is placed on a 0.5 m diameter rotating table, which allows rotation with angular velocity $\tilde{\Omega}^G$ up to ± 60 r.p.m.

The paper is organized as follow. In § 2, we focus on the cylindrical geometry: theoretical results both from the global and short-wavelength analyses are presented and compared quantitatively with our experiments. We demonstrate that the global rotation allows excitation of various modes of the elliptical instability in a given cylinder with a fixed aspect ratio $\tilde{H}/\tilde{R}$, in contrast to previous experiments where the length of the cylinder was adjusted so as to excite a given resonance (e.g. Eloy *et al.* 2003). In § 3, we then show how the global rotation allows the tuning of various eigenmodes of the sphere, hence the excitation of complex elliptical instabilities in addition to the standard spin-over observed without Coriolis effects (e.g. Lacaze *et al.* 2006). To the best of our knowledge, this is the first time these complexe modes have been experimentally observed, except for the twin-vortex mode mentioned by Boubnov (1978). Finally in the last section, the main results of the paper are summarized and some geophysical and astrophysical consequences of our study are briefly discussed.

2. Theoretical and experimental study in the cylinder

2.1. *Theoretical approaches*

2.1.1. *Inviscid global study*

The elliptical instability mechanism has been reviewed in Kerswell (2002). It is associated with the parametric resonance of two inertial waves of the undistorted circular flow induced by the underlying strain field (e.g. Waleffe 1990; Kerswell 2002). For small deformations, the global (or normal-mode) theory permits the conditions of resonance for a given geometry to be calculated explicitly and provides information on the structure of the eigenmodes. Results for the elliptical instability in a cylinder with Coriolis effects have been obtained by Kerswell (1994): they are here summarized and adapted to our particular experimental situation.

In the following, variables are non-dimensionalized using the characteristic time scale $1/\tilde{\Omega}^F$ and the characteristic length scale $\tilde{R}$. We work in the frame rotating with the rotating table, i.e. in the frame where the elliptical deformation is stationary. In the undistorted cylinder, we can look, in cylindrical coordinates, for normal neutral modes of the form

$$(\boldsymbol{u}, p) = (u(r)\cos(\gamma z), v(r)\cos(\gamma z), w(r)\sin(\gamma z), p(r)\cos(\gamma z))\mathrm{e}^{\mathrm{i}(m\theta-\omega t)}, \tag{2.1}$$

where the vertical boundary conditions simply imply

$$\gamma = n\pi\tilde{R}/\tilde{H}, \tag{2.2}$$

n being an integer corresponding to the number of axial half–periods. Following Waleffe (1990) and taking into account the additional Coriolis term $2\Omega^{\mathrm{G}}\times\boldsymbol{u}$ coming from the global rotation, the linearized Euler equations can be reduced to a single

Bessel equation for the axial velocity w:

$$r\frac{\mathrm{d}}{\mathrm{d}r}\left(r\frac{\mathrm{d}w}{\mathrm{d}r}\right)+(\beta^2r^2-m^2)w=0, \tag{2.3}$$

where the radial wavenumber β is given by

$$\beta=\gamma\sqrt{\frac{4(1+\Omega^G)^2}{\lambda^2}-1} \tag{2.4}$$

and $\lambda=\omega-m$ is the mode frequency in the frame rotating with the flow. If we enforce the radial boundary condition $u(1)=0$, i.e.

$$r\frac{\mathrm{d}w}{\mathrm{d}r}+\frac{2m(1+\Omega^G)}{\lambda}w=0 \text{ at } r=1, \tag{2.5}$$

on the regular solution of (2.3) $w=J_m(\beta r)$, we obtain the dispersion relation between the frequency λ (or ω in the non-rotating frame) and the axial wavenumber γ for given values of m and Ω^G. The radial wavenumber β is found to be discretized. There are infinitely many branches associated with each wavenumber, which can be labelled by the number of zeros of the radial velocity eigenmode. According to (2.4), they lie in the interval

$$|\lambda|\leqslant|2(1+\Omega^G)|. \tag{2.6}$$

As explained in Kerswell (2002), the elliptical instability results from a triadic resonance between the elliptical deformation and two normal modes (m_a,γ_a,ω_a) and (m_b,γ_b,ω_b) of the undistorted circular flow. The conditions of resonance are simply

$$m_b=m_a+2,\quad \gamma_a=\gamma_b,\quad \omega_a=\omega_b. \tag{2.7}$$

According to (2.6), this can only be achieved if

$$\Omega^G\geqslant-1/2 \text{ or } \Omega^G\leqslant-3/2, \tag{2.8}$$

i.e. there exists a forbidden band for Ω^G between $-3/2$ and $-1/2$ where the elliptical instability cannot develop.

In the inviscid framework, numerous resonances are unstable. But combinations of normal modes having the same radial structure are significantly more amplified than the others and are in fact the only ones observed in experiments (Eloy, Le Gal & Le Dizès 2000): they are named principal modes and denoted (m_a,m_b,i), where i corresponds to the label of the branches involved in the resonance.

One can notice that the normal mode equations (2.3)–(2.5) are similar to those without global rotation (e.g. Waleffe 1990), provided the frequency λ is replaced by

$$\tilde{\lambda}=\lambda/(1+\Omega^G). \tag{2.9}$$

Hence, dispersion relation curves given for instance by Eloy *et al.* (2003) remain unchanged, representing $\tilde{\omega}=\tilde{\lambda}+m$ instead of $\omega=\lambda+m$ (see figure 2). The condition for resonance $\omega_a=\omega_b$ is now

$$\tilde{\omega}_b-\tilde{\omega}_a=\frac{2\Omega^G}{1+\Omega^G}. \tag{2.10}$$

As illustrated in figure 3, resonances with various structures can be excited in a given cylinder by changing the global rotation rate Ω^G only. When Ω^G goes toward $-1/2^+$ or $-3/2^-$, numerous possible resonances are very close and the wavenumber of the instability rapidly increases: experiments will tell us which mode is actually

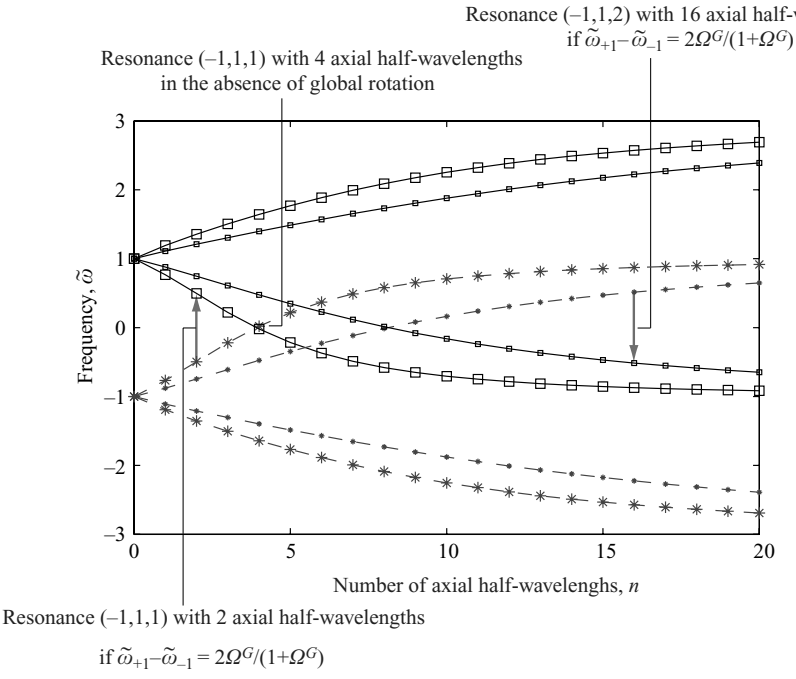

FIGURE 2. Dispersion relation points of the $m=-1$ (stars) and $m=1$ (squares) eigenmodes for the first and second smaller radial wavenumbers β (large and small symbols respectively) in the cylinder of height $\tilde{H}=21.4\,\mathrm{cm}$ used in the experiments, depending on the number n of axial half-wavelengths. For each given axial and radial structure, the corresponding resonance is excited provided the distance between the $m=1$ and $m=-1$ curves is given by (2.10): three examples with or without global rotation are shown.

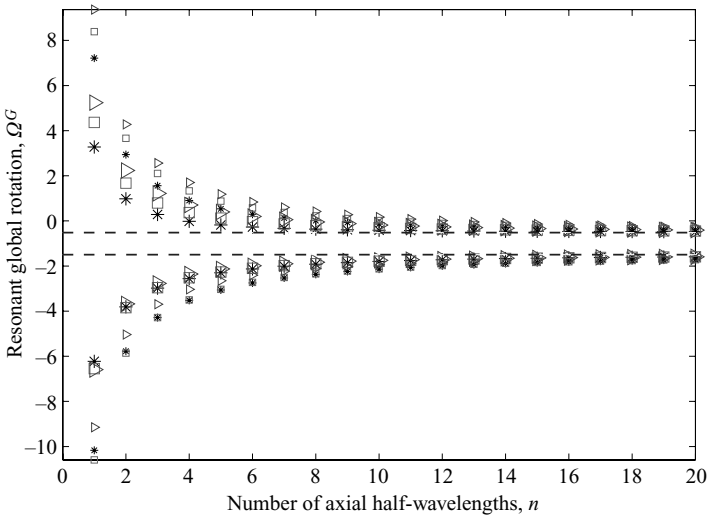

FIGURE 3. Theoretical predictions for the resonant values of the global rotation rate as a function of the number n of axial half-periods in our experimental cylinder of height $\tilde{H}=21.4\,\mathrm{cm}$: large stars stand for the modes $(-1, 1, 1)$, small stars for the modes $(-1, 1, 2)$, large squares for the modes $(0, 2, 1)$, small squares for the modes $(0, 2, 2)$, large triangles for the modes $(1, 3, 1)$ and small triangles for the modes $(1, 3, 2)$. The forbidden band $-3/2<\Omega^G<-1/2$ is delimited by the dashed lines.

selected. On the contrary, discretized instabilities with relatively small wavenumbers are expected further away from the forbidden band $-3/2 < \Omega^G < -1/2$ and will be independently excited in our experiment.

2.1.2. *Local approach*

In addition to the conditions for resonance given by the global approach, the local approach allows the analytical determination of the growth rate of the instability. It is based on the inviscid short-wavelength Lagrangian theory developed by Bayly (1986) and Craik & Criminale (1986), then generalized by Friedlander & Vishik (1991) and Lifschitz & Hameiri (1991). In this approach, perturbations are assumed to be sufficiently localized to be advected along flow trajectories and are sought in the form of local plane waves

$$(u, p) = (u(t), p(t))\mathrm{e}^{\mathrm{i}\boldsymbol{k}(t)\cdot\boldsymbol{r}}. \tag{2.11}$$

This method has been applied to the elliptical instability with global rotation by Le Dizès (2000). Here, we briefly recall his work, then include the boundary viscous effects, and present the results in a way directly relevant to our experiments.

In the frame rotating at the global rotation rate Ω^G (i.e. where the shear is stationary), the two-dimensional basic flow in our container is described at leading order in ε by the stream function (in polar coordinates)

$$\Psi = -\frac{r^2}{2}(1 - \varepsilon\cos(2\theta)), \tag{2.12}$$

where ε is the eccentricity of the elliptical streamline. Replacing Ψ in the linearized Euler equations by its expression (2.12) and decoupling the system in space and time, immediately gives the wavevector

$$\boldsymbol{k}(t) = k\left(\frac{\sin(a)}{\sqrt{A}}\cos(\chi t), \sin(a)\sqrt{A}\sin(\chi t), \cos(a)\right), \tag{2.13}$$

where k is a constant, $A = \sqrt{(1+\varepsilon)/(1-\varepsilon)}$ is the ellipticity, $\chi = \sqrt{1-\varepsilon^2}$, and a is the angle between the flow rotation axis and the wavevector. Writing $\Omega^G = \Omega_0^G + \varepsilon\Omega_1^G + O(\varepsilon^2)$ and $a = a_0 + \varepsilon a_1 + O(\varepsilon^2)$, the perturbation analysis for small eccentricity gives at order 0 in ε the frequency f of the plane wave solution of the linearized Euler equations:

$$f = \pm 2\left(1 + \Omega_0^G\right)\cos(a_0). \tag{2.14}$$

According to Le Dizès (2000), an elliptical instability is possible if the forcing terms due to the elliptical deformation oscillate at the same frequency as the inertial wave, which means in our case if $f = 1$. From (2.14), this is only possible if $\Omega_0^G \geqslant -1/2$ or $\Omega_0^G \leqslant -3/2$, in agreement with the result (2.8) from the global analysis. Then, at order 1 in ε, the solvability conditions directly determine the exponential growth rate of the elliptical instability (Le Dizès 2000):

$$\sigma = \sqrt{\left(\frac{3 + 2\Omega^G}{4(1+\Omega^G)}\right)^4 \varepsilon^2 - (1 - 2|1+\Omega^G|\cos(a))^2}. \tag{2.15}$$

Assuming that the viscous dissipation is of order ε, viscous effects on the localized perturbations can be easily taken into account by adding the viscous damping rate (Craik & Criminale 1986)

$$-k^2 Re^{-1}. \tag{2.16}$$

to the expression (2.15). Here Re is the Reynolds number defined by $Re = \tilde{\Omega}^F \tilde{R}^2/\nu$ and ν the kinematic viscosity of the fluid. Viscous effects on the surface of the container for plane wave perturbations can be estimated using the work of Kudlick (1966) (see also Kerswell & Barenghi 1995), introducing corrections of order $Re^{-1/2}$. For the $(-1, 1)$ resonance in the cylindrical container, the growth rate is finally given by

$$\sigma = \sqrt{\left(\frac{3+2\Omega^G}{4(1+\Omega^G)}\right)^4 \varepsilon^2 - \left(1 - 2|1+\Omega^G|\cos(a) + \mathrm{Im}(s_v)Re^{-1/2}\right)^2} - Re(s_v)Re^{-1/2} - k^2 Re^{-1}, \quad (2.17)$$

where $\mathrm{Im}(s_v)$ and $Re(s_v)$ stand respectively for the imaginary part and the real part of the boundary viscous coefficient determined for the cylinder:

$$s_v = \frac{4-x^2}{4\sqrt{2}(1+k^2-x/2)}\left(\frac{(1+\mathrm{i})(2-x)(1+k^2-2x/(2-x))}{\sqrt{2+x}} + \frac{(1-\mathrm{i})(2+x)(1+k^2-2x/(2+x))}{\sqrt{2-x}} + (1+\mathrm{i})(1+k^2)\frac{\tilde{H}}{\tilde{R}}\sqrt{x}\right)(1+\Omega^G)^{1/2}\frac{\tilde{R}}{\tilde{H}}, \quad (2.18)$$

where

$$x = \left|\frac{\Omega^G}{1+\Omega^G} - 1\right|. \quad (2.19)$$

This complex formula can be used to interpret the experiments, provided the local parameters (k, a) are related to the global properties of the instability. This is immediately clear when looking at the coupling between the symmetrical modes $m = -1$ and $m = 1$, which possess both the same axial wavenumber γ and the same radial wavenumber β defined by (2.2) and (2.4). In the limit of large k relevant to the local approach, (k, a) are simply

$$k = \sqrt{\beta^2+\gamma^2}, \cos(a) = \frac{\gamma}{\sqrt{\beta^2+\gamma^2}}. \quad (2.20)$$

For given values of $(\tilde{R}, \tilde{H}, \tilde{\Omega}^F, \nu, \varepsilon)$ and for a chosen radial structure defined by β, (2.17) determines bands of instability depending on the global rotation rate Ω^G. Each band corresponds to a given axial structure determined by the number n of axial half-periods. It is more or less centred on the perfect resonance given by the global approach, but a small detuning of typically ± 0.05 on Ω^G for $Re \sim 10^3$ is allowed. Two examples of these theoretical predictions for the simplest but dominant mode $(-1, 1, 1)$ are shown in figure 4, together with our experimental data. The resonance bands are separated by large regions with no resonance for $\Omega^G \geqslant 0$ (i.e. for cyclones). For $\Omega^G \leqslant 0$ (i.e. for anticyclones), they progressively overlap, and immediatly disappear once the global rotation rate reaches a critical value $\Omega^G_c \sim -1/2$.

2.2. *Experimental study*

A series of experiments was performed using a cylinder of height $\tilde{H} = 21.4\,\mathrm{cm}$ and eccentricity $\varepsilon = 0.085$, systematically changing $\tilde{\Omega}^F$ and $\tilde{\Omega}^G$ in order to test the various conclusions of the two complementary theoretical approaches. We want to observe experimentally (i) the selective excitation of a given resonance depending on Ω^G, as indicated by the global theory, and (ii) the rapid increase in wavenumber and growth rate as well as the sudden disappearance of the instability when decreasing

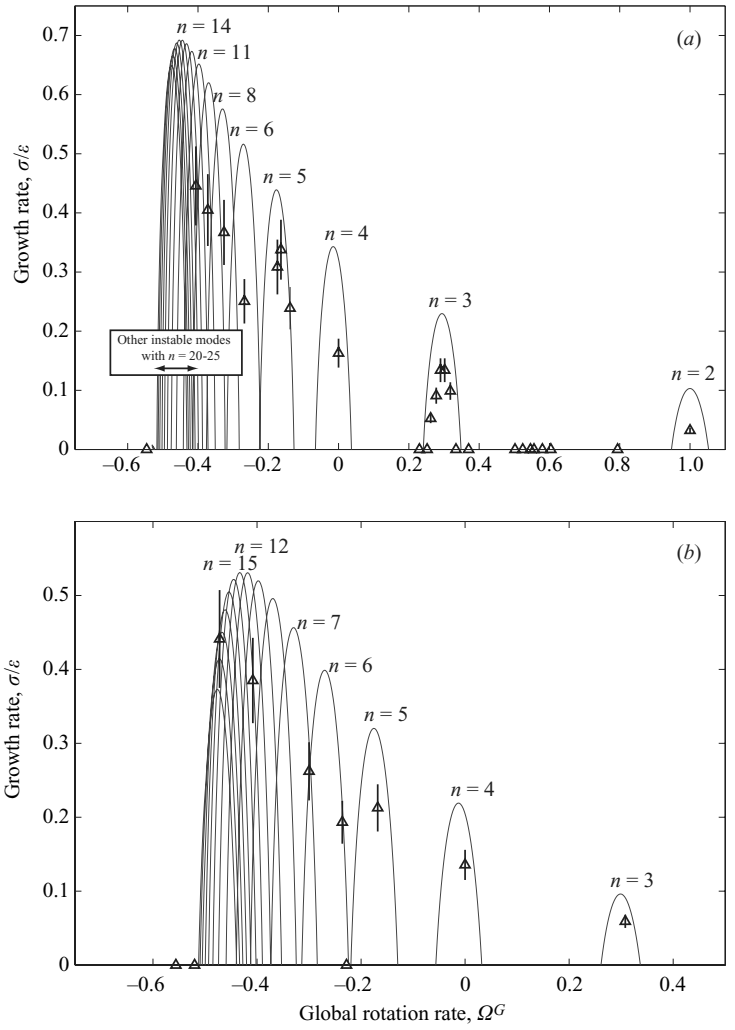

FIGURE 4. Viscous growth rate of the elliptical instability mode $(-1, 1, 1)$ determined by the local analysis as a function of the global rotation rate Ω^G for a given cylinder of radius $\tilde{R} = 2.75\,\text{cm}$, height $\tilde{H} = 21.4\,\text{cm}$, eccentricity $\varepsilon = 0.085$, filled with water ($\nu = 10^{-6}\,\text{m}^2\,\text{s}^{-1}$): (*a*) $\tilde{\Omega}^F = 0.505 \pm 0.005\,\text{Hz}$ ($Re = 2.40 \times 10^3$) and (b) $\tilde{\Omega}^F = 0.255 \pm 0.002\,\text{Hz}$ ($Re = 1.21 \times 10^3$). Triangles stand for experimental measurements and solid lines for theoretical predictions. The predicted number n of axial half-wavelengths increases by 1 from the right to the left on each resonant band, starting from $n = 2$ in (*a*) and $n = 3$ in (*b*); measured values are indicated above each experimental point. Note that in (*a*), additional resonances were observed for Ω^G in the range $[-0.507; -0.403]$; nevertheless, because of their small wavelength and their rapid growth rate, quantitative measurements were not accurate.

Ω^G toward $-1/2$, as indicated by the local theory. Our protocol is the same for all the experiments presented here. First, we set the global rotation to its assigned value and wait for solid-body rotation to take place in the container. Then we start the rotation of the container: a spin-up phase first occurs, before the possible development of an instability. The flow is visualized in the frame rotating at $\tilde{\Omega}^G$ using a light plane illuminating the container that is filled with water seeded by kalliroscope particles. The elongated and flat shape of these reflective flakes forces them to align in the strain

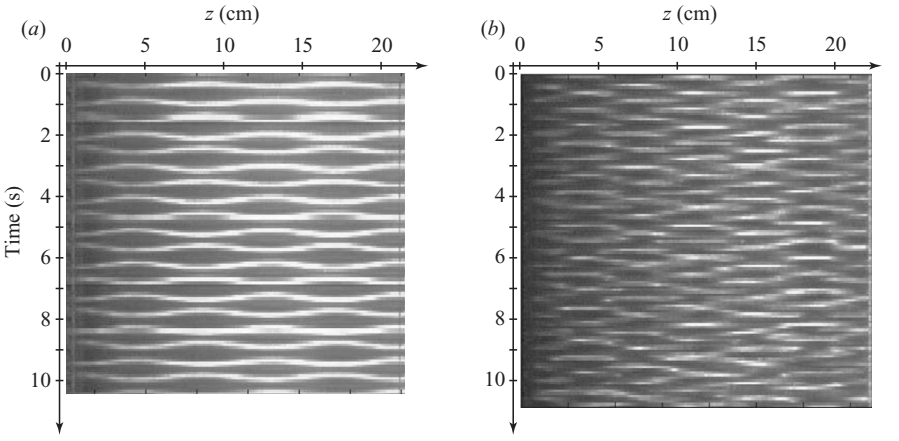

FIGURE 5. Spatiotemporal diagrams obtained by extracting the same line parallel to the rotation axis in each image of a given video sequence: (*a*) mode (0,2,1) with $n = 5$ shown in figure 7, with $\tilde{\Omega}^F = 1.000\,\text{Hz}$ ($Re = 4.75 \times 10^3$) and $\tilde{\Omega}^G = 0.110\,\text{Hz}$; (*b*) mode (1,3,1) with $n = 6$ shown in figure 7, with $\tilde{\Omega}^F = 1.000\,\text{Hz}$ ($Re = 4.75 \times 10^3$) and $\tilde{\Omega}^G = 0.198\,\text{Hz}$. z stands for the distance along the rotation axis, from $z = 0$ to $z = 21.4\,\text{cm}$.

field and allows visualization of the velocity field. In particular, the rotation axis and its undulations are clearly visible. The experimental (integer) wavenumber is then simply determined by dividing the cylinder length by the mean measured wavelength of the identical structures along the axis, and the mode frequency is measured from spatiotemporal diagrams such as those shown in figure 5.

All experiments presented are carried out near the instability threshold: the characteristic growth time is then much larger than the spin-up time and decorrelation of the two phenomena is expected. In the immediate vicinity of threshold, the unstable mode reaches a stable saturation state. For larger values of the Reynolds number, the mode grows continuously, until it breaks down into small scales. In some cases, the flow relaminarizes through viscous dissipation and a new cycle starts, as also noticed by Malkus (1989) and Eloy *et al.* (2000).

2.2.1. *Observed resonances in the cylinder*

A series of experiments was first performed to observe the various possible resonances in the cylinder by changing $\tilde{\Omega}^F$ and $\tilde{\Omega}^G$ only. Results are reported in tables 1 and 2, and corresponding pictures are shown in figures 6 and 7. Good agreement is found with the linear inviscid global approach: stationary mode $(-1, 1, 1)$ with a sinusoidal rotation axis and various wavelengths (figure 6) as well as other more exotic modes recognizable by their complex radial structure (figure 7) and/or by their periodic behaviour (figure 5) can be selected by changing the dimensionless ratio Ω^G only, provided the Reynolds number is large enough. Only two limitations are to be noted. First, pulsations of oscillatory modes are always slightly overestimated by the linear theory, as also observed by Eloy *et al.* (2003) in the non-rotating case. This is presumably due to a frequency detuning induced by nonlinear effects, as explained by Waleffe (1990). Secondly, the wavenumber of the mode $(-1, 1, 1)$ for $n \geqslant 7$ typically (i.e. for $\Omega^G < -0.29$ typically) does not exactly match predictions of the normal-mode analysis: this is due to the overlapping of the various possible

Theory		Experiments			
Ω^G	n	$\tilde{\Omega}^F$ (Hz)	$\tilde{\Omega}^G$ (Hz)	Ω^G	n
0.980	2	0.506	0.499	0.968	2
0.285	3	0.255	0.077	0.302	3
		0.500	0.113	0.226	3
		0.503	0.145	0.288	3
		0.504	0.126	0.250	3
		0.504	0.151	0.300	3
		0.506	0.139	0.275	3
		0.506	0.131	0.259	3
		0.506	0.159	0.314	3
		0.506	0.167	0.330	3
		1.002	0.250	0.2495	3
−0.0194	4	0.257	0	0	4
		0.503	0	0	4
−0.178	5	0.254	−0.042	−0.165	5
		0.505	−0.087	−0.172	5
		0.505	−0.082	−0.162	5
		0.505	−0.069	−0.137	5
−0.270	6	0.255	−0.059	−0.231	6
		0.255	−0.057	−0.2235	6
		0.507	−0.134	−0.264	6
		0.255	−0.075	−0.294	7
−0.328	7	0.508	−0.163	−0.321	9
−0.367	8	0.508	−0.186	−0.366	11
−0.394	9	0.507	−0.203	−0.400	14
		0.253	−0.102	−0.403	12
−0.455	14	0.507	−0.231	−0.456	20
−0.465	16	0.255	−0.118	−0.463	15
		0.255	−0.118	−0.463	18
−0.467	28	0.507	−0.237	−0.4675	20
−0.500	∞	0.500	−0.249	−0.498	25
		0.507	−0.257	−0.507	25

TABLE 1. Theoretical predictions for the mode $(-1, 1, 1)$ of instability and comparison with experimental results for a cylinder of radius $\tilde{R} = 2.75\,\text{cm}$, height $\tilde{H} = 21.4\,\text{cm}$, eccentricity $\varepsilon = 0.085$ and various values of the global rotation Ω^G. Typical accuracy on $\tilde{\Omega}^F$ and $\tilde{\Omega}^G$ is $\pm 0.005\,\text{Hz}$. n stands for the (integer) number of axial half-wavelengths. Pictures of the corresponding experiments are shown in figure 6. Theoretical predictions correspond to the closest perfect resonance given by the global analysis. As shown by the local analysis, non-perfect resonances due to a small detuning are theoretically possible and experimentally observed; in particular, elliptical instability takes place slightly below the threshold $\Omega^G = -1/2$ determined by the global approach.

resonances and to the viscous damping of the smallest structures, as suggested by the short-wavelength analysis (see figure 4).

When several theoretical resonances are close together, we sometimes observed the superposition or the succession in time of the different modes. The precise mechanism governing this phenomenon is probably controlled by nonlinear processes and its description is beyond the scope of this paper. Note however that there is a great tendency for the mode with the simplest axial and radial structures to occur alone. In particular, in the range $-1/2 < \Omega^G < -0.13$ where resonance bands overlap (see figure 4), the mode $(-1, 1, 1)$ is always the only one excited.

	Theory			Experiments				
Mode	Ω^G	n	ζ	$\tilde{\Omega}^F$ (Hz)	$\tilde{\Omega}^G$ (Hz)	Ω^G	n	ζ
(−1,1,2)	0.533	5	0	1.000	0.440	0.440	5	0
				1.000	0.535	0.535	5	0
(−1,1,2)	0.131	7	0	0.499	0.054	0.108	7	0
				0.508	0.070	0.138	7	0
(0,2,1)	0.794	3	1.08	1.000	0.794	0.794	3	1.01
(0,2,1)	0.368	4	1.06	1.006	0.377	0.375	4	1.06
				1.002	0.368	0.367	4	1.01
(0,2,1)	0.125	5	1.05	0.508	0.070	0.138	5	0.996
				1.000	0.110	0.110	5	0.965
				0.748	0.084	0.112	5	0.972
(0,2,2)	0.5785	6	1.03	1.374	0.801	0.5835	6	0.968
(0,2,2)	0.220	8	1.03	0.996	0.222	0.2225	8	0.962
(1,3,1)	0.399	5	2.08	1.92	0.801	0.417	5	2.01
				1.004	0.418	0.399	5	1.94
(1,3,1)	0.198	6	2.06	1.000	0.198	0.198	6	2.00
(1,3,2)	0.416	8	2.04	1.000	0.415	0.415	8	1.98

TABLE 2. As in table 1 but for the other observed modes of instability. Corresponding pictures are shown in figure 7. ζ stands for the frequency of the elliptical resonance: typical precision on the experimental values is 10 %.

2.2.2. *Quantitative analysis of the mode* (−1, 1, 1)

The stationary mode (−1, 1, 1) is especially interesting since its growth rate can be determined experimentally: from sequences of images, we measure the maximum amplitude of the sinusoidally deformed rotation axis; its temporal evolution is then fitted with an exponential growth, which can be compared to the exponential growth rate determined by the local theory (2.17). An example of data fitting is shown in figure 8 (see also Eloy *et al.* 2003). The variations of the growth rate with respect to Ω^G are presented in figure 4 together with the viscous theoretical estimate (2.17). First, one can see that the threshold for instability agrees with the theory, with for instance the sharp disappearance of resonant modes at $\Omega_c^G = -0.520 \pm 0.004$ for $\tilde{\Omega}^F = 0.505 \pm 0.005$ Hz. Measurements of the growth rate qualitatively agree with the theory, regarding the general increasing trend when Ω^G decreases toward $-1/2$, and also regarding the specific shape of one resonance band (see for instance in figure 4*a* the band around $\Omega^G = 0.285$ that we have explored in detail). Quantitatively, orders of magnitude also agree, but theoretical values always overestimate experimental values. Three main explanations can be provided. First, nonlinear effects were not taken into account in the theory, but are expected to be stabilizing (Eloy *et al.* 2003). Then, recall that the theoretical estimate is based on a short-wavelength (i.e. large k) asymptotic analysis: the discrepancy could therefore be associated with finite-k effects. One can in particular see that the systematic error significantly decreases when going toward $\Omega^G = -1/2$, i.e. when the number of observed axial structures rapidly increases, and the experiment more closely agrees with the analytical limit. The last source of discrepancy is experimental. In our set-up, rollers only deform the central part of the cylinder: consequently, the eccentricity changes along the axis, which directly influences the growth rate, as suggested by (2.17). This is especially important for large n, where instabilities are localized in the deformed part of the cylinder only, as shown for instance in the last picture of figure 6. To quantify this

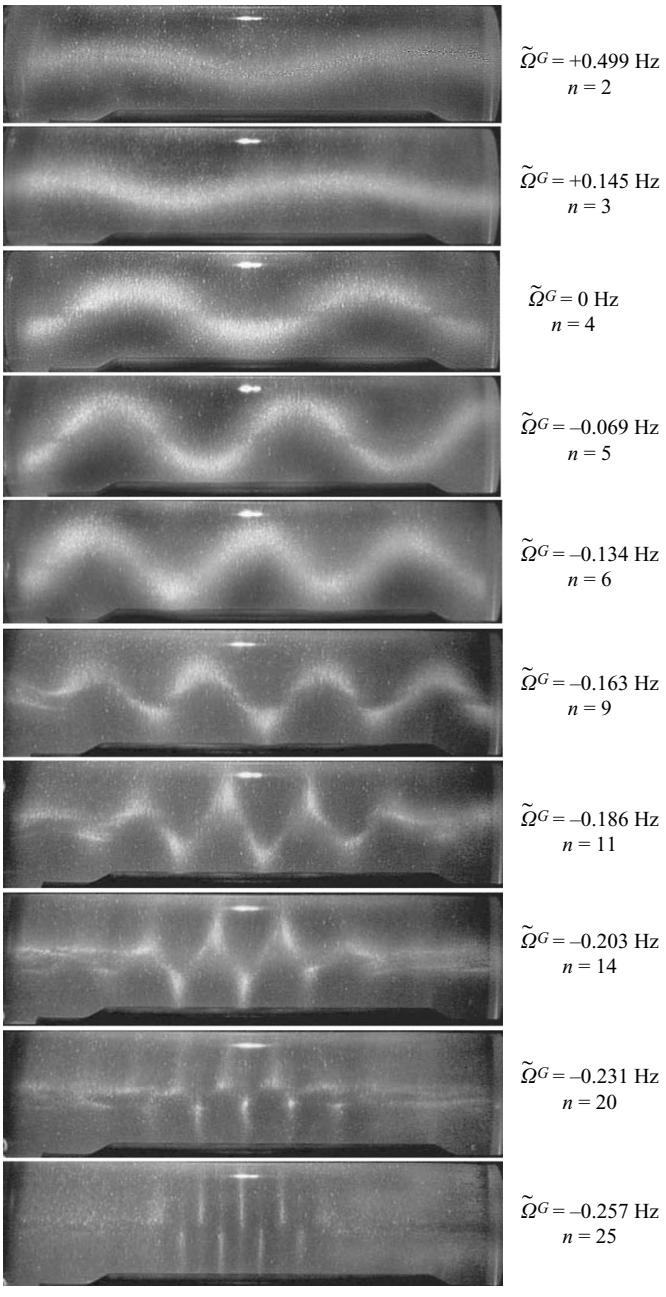

FIGURE 6. Variation of the wavelength of the mode $(-1, 1, 1)$ versus the global rotation $\tilde{\Omega}^G$ for a given cylinder of radius $\tilde{R} = 2.75$ cm and height $\tilde{H} = 21.4$ cm with an eccentricity $\varepsilon = 0.085$ rotating at $\tilde{\Omega}^F = 0.505 \pm 0.005$ Hz ($Re = 2.40 \times 10^3$). Here, all pictures have been rotated by 90° for convenience.

effect, we performed two experiments with $\tilde{\Omega}^F = 0.993$ Hz and $\tilde{\Omega}^G = 0$ Hz with rollers of height 13.4 cm (i.e. the standard rollers) and 4.9 cm respectively: the measured growth rate then decreases from $0.090\,\mathrm{s}^{-1}$ to $0.052\,\mathrm{s}^{-1}$, which qualitatively confirms

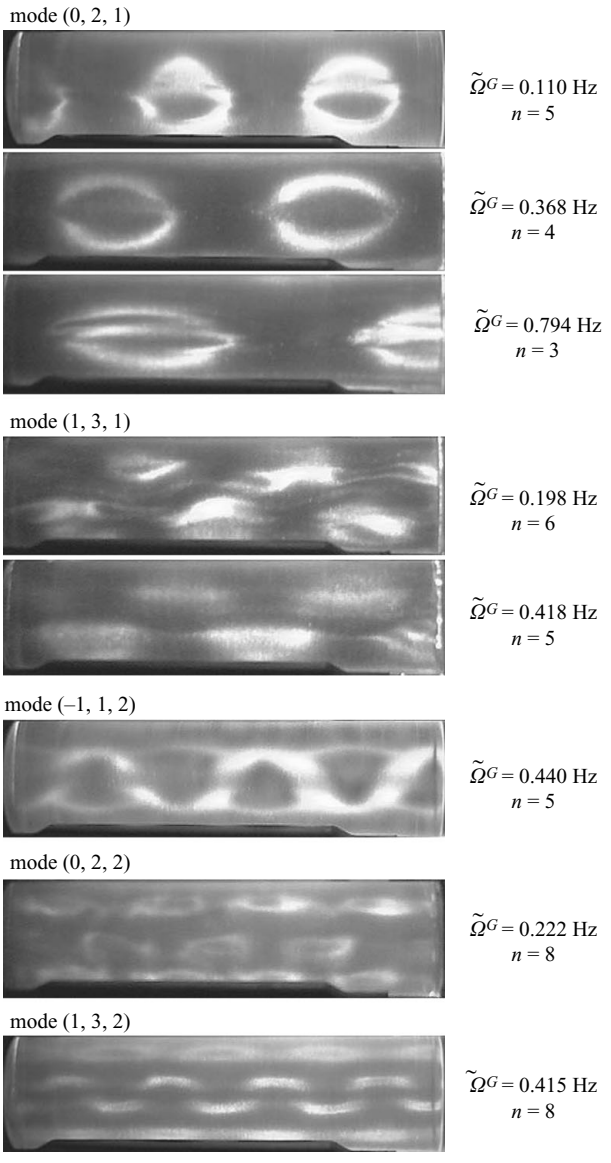

FIGURE 7. Pictures of the observed modes of elliptical instability depending on the global rotation $\tilde{\Omega}^G$ for a given cylinder of radius $\tilde{R} = 2.75$ cm and height $\tilde{H} = 21.4$ cm with an eccentricity $\varepsilon = 0.085$ rotating at $\tilde{\Omega}^F = 1.001 \pm 0.005$ Hz ($Re = 4.76 \times 10^3$). Here, all pictures have been rotated by 90° for convenience.

the suggested correction, but also demonstrates that the induced correction is not directly proportional to some mean value of the deformation.

Finally, note that the main limitation of our experimental device comes from the rotation rate of the rotating table (up to ± 1 Hz only). Taking into account viscous dissipation, it was not possible to choose $\tilde{\Omega}^F$ and $\tilde{\Omega}^G$ to explore the range below $\Omega^G = -1$. We can only expect, in the light of the good agreement between theoretical predictions and experiments for $\Omega^G \geqslant -1$, that this will also be the case for $\Omega^G < -1$, and in particular, that instabilities will reappear for $\Omega^G \leqslant -3/2$.

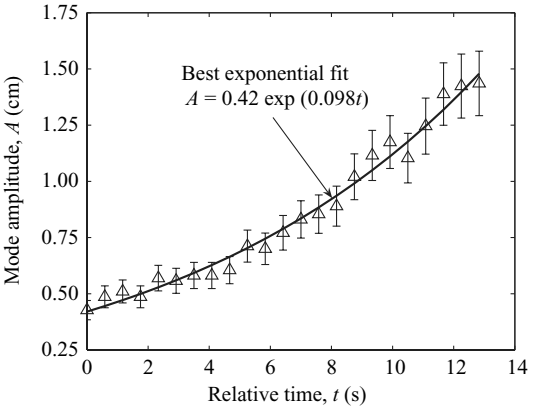

FIGURE 8. Initial evolution over time of the maximum radial amplitude of the mode $(-1, 1, 1)$ in the cylinder of radius $\tilde{R} = 2.75\,\text{cm}$ and height $\tilde{H} = 21.4\,\text{cm}$ with an eccentricity $\varepsilon = 0.085$ rotating at $\tilde{\Omega}^F = 0.508\,\text{Hz}$ ($Re = 2.41 \times 10^3$) with a global rotation of $\tilde{\Omega}^G = -0.163\,\text{Hz}$. The best exponential fit indicates a growth rate $\sigma = 0.098\,\text{s}^{-1}$.

3. Theoretical and experimental study in the sphere

3.1. *Inviscid global study*

The eigenmodes of the sphere have been studied in the non-rotating case by Greenspan (1968). His study can be modified to take into account an additional Coriolis force, similarly to what has been done for the cylindrical case in § 2.1.1. The global rotation leads to exactly the same changes as in the cylinder and the algebra is not detailed here. We simply show in figure 9 the dispersion relation points for the $m = -1$ and $m = 1$ eigenmodes, representing the evolution of $\tilde{\omega} = (\omega - m)/(1 + \Omega^G) + m$ (rather than ω in the non-rotating case) as a function of the spatial wavenumber.

The problem of resonances is more complex than in the cylinder. There, as demonstrated by Eloy *et al.* (2003), the best coupling appears between modes having the same radial and axial structures. In the sphere, as shown in Greenspan (1968), the modes are indexed by the degree d of the Legendre polynomial determining their spatial structure, $n = d - |m|$ being equivalent to a spatial wavenumber; but the analytical approach does not provide a direct and independent quantification of the axial and radial structures of the eigenmodes. It is thus more difficult to determine the general conditions for the best resonance, and additional theoretical work is currently in progress.

Nevertheless, in the context of the present study, we simply focus on the coupling between the lowest points of the $m = 1$ eigenmode and the highest points of the $m = -1$ eigenmode, corresponding to a principal mode $(-1, 1, 1)$ in the cylinder: both modes have a single radial structure and the number of axial half-wavelengths is directly given by n. Then, conditions for resonance are simply $n_{-1} = n_1$ and $\omega_{-1} = \omega_1$, or $\tilde{\omega}_1 - \tilde{\omega}_{-1} = 2\Omega^G/1 + \Omega^G$, as illustrated in figure 9. In contrast to the non-rotating case where the only exact resonance in the sphere leads to the spin-over mode (i.e. a solid-body rotation around the axis of maximum strain, see Lacaze *et al.* 2004), more complex instabilities can be triggered by the global rotation, as sketched in figure 10. We will now show that these unstable modes $(-1, 1, 1)$ are indeed prevalent in the experiments.

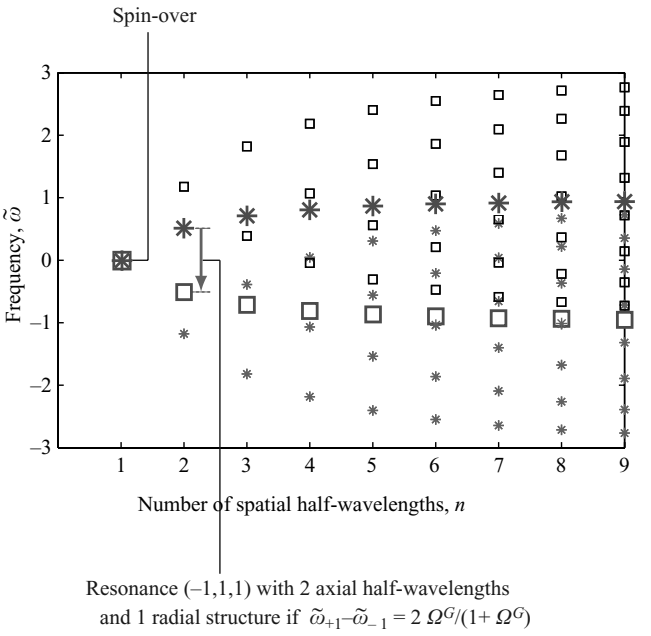

FIGURE 9. Dispersion relation points for $m=-1$ (stars) and $m=1$ (squares) in a sphere. This graph resembles the one presented in figure 2 for the cylinder, replacing the number n of axial half-wavelengths by the number n of spatial half-wavelengths (see the complete resolution in Greenspan 1968). Large symbols stand for the eigenmodes with the simplest radial structure: n is then the number of axial half-wavelengths, as for the cylinder. Using the same notation as for the cylinder, a resonance $(-1, 1, 1)$ is excited providing the distance between the $m=1$ and $m=-1$ points is given by (2.10): examples for the non–rotating case (i.e. the spin-over) and for a rotating case are explicitly shown. Resonances between eigenmodes with the simplest radial structure are sketched in figure 10; they are the only ones studied in the present paper.

3.2. *Observed resonances in the sphere*

A series of experiments was performed in the sphere of radius $\tilde{R}=2.175\,\text{cm}$ with a fixed eccentricity $\varepsilon=0.20$, systematically changing $\tilde{\Omega}^G$ and $\tilde{\Omega}^F$ to excite various resonances. In the explored range $-0.6<\Omega^G<0$, we observed the same behaviour as in the cylinder: the principal modes $(-1, 1, 1)$ which possess a single radial structure are the dominant modes, and when Ω^G decreases towards $-1/2$, the number of axial structures as well as the growth rate of the instability rapidly increase (see figure 11), until the instability suddenly disappears in the vicinity of $\Omega^G\sim-1/2$. As shown in table 3, excited modes with $n\leqslant 5$ are in good agreement with analytical predictions for Ω^G in a resonance band typically of ±0.03 around the theoretical perfect-resonance value. We think that the discrepancies for $n\geqslant 5$ are due to the overlapping of resonant bands, as observed in the cylinder (see figure 4). With our experimental device, the visualization in the sphere was not precise enough to allow a systematic measurement of the growth rate of the elliptical instability, but we determined experimentally the viscous threshold of instability for two given values of the flow rotation rate: $\Omega_c^G=-0.557\pm0.004$ for $\tilde{\Omega}^F=0.501\pm0.005\,\text{Hz}$ and $\Omega_c^G=-0.551\pm0.004$ for $\tilde{\Omega}^F=0.747\pm0.005\,\text{Hz}$. We recall that in the absence of global rotation, the only perfect resonance and the only observed mode in the vicinity of threshold (i.e. at low Reynolds number) is the spin-over, corresponding to a single additional rotation around the axis of maximum strain (see Lacaze *et al.* 2004).

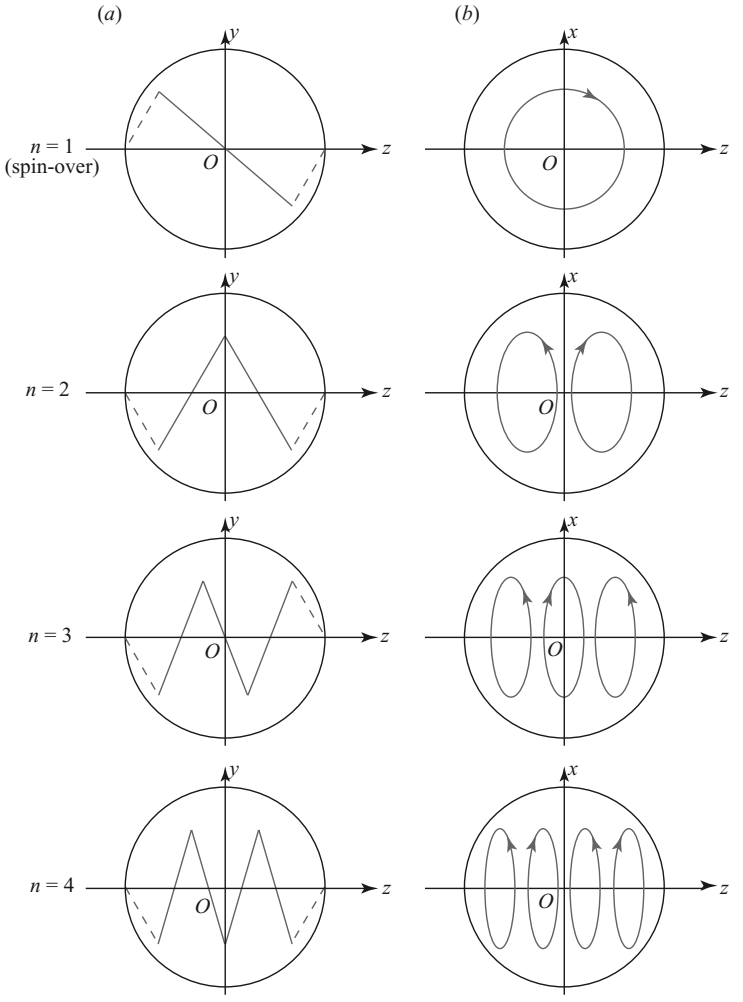

FIGURE 10. Sketches of the flow structure in a sphere associated with the resonance $(-1, 1, 1)$ for various n. The instability modes have a single radial structure and the number of axial half-wavelengths is directly given by n. (*a*) Effective rotation axis in the (O, y, z) plane resulting from the superimposition of the base flow rotation and of the instability mode. Dashed lines stand for viscous boundary layers, where the fluid motion progressively matches the rigid container rotation. (*b*) Typical streamlines in the (O, x, z) plane of the instability mode. $n = 1$ corresponds to the spin-over mode (Lacaze *et al.* 2004); $n = 2$ corresponds to the twin-vortex mode of Boubnov (1978); and to the best of our knowledge, the other modes have not yet been observed experimentally.

4. Conclusion

In this paper, we have presented an analytical and experimental study of the influence of the Coriolis force on the elliptical instability. For a given container – either cylindrical with a fixed aspect ratio $\tilde{H}/\tilde{R}$ or spherical – the global rotation rate allows various resonances to be selected, in good agreement with the global theory. In particular, we have observed in the sphere numerous complex stationary modes at relatively low values of the Reynolds number, in addition to the simple spin-over that takes place in the non–rotating case. For both the cylinder and the sphere, on

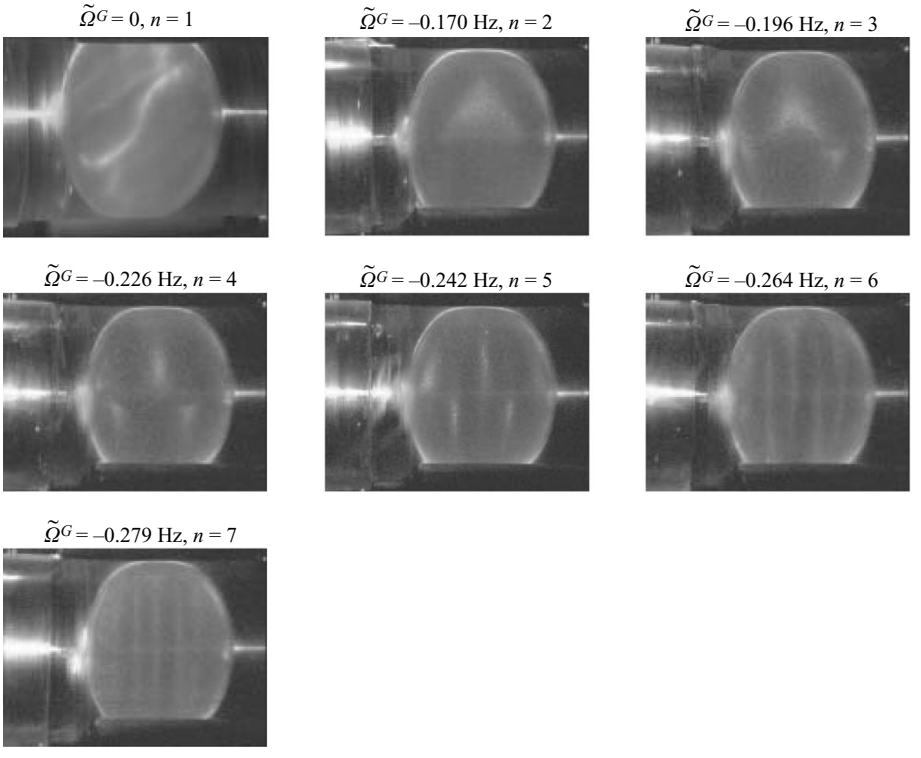

FIGURE 11. Pictures of the flow structure associated with an instability mode $(-1, 1, 1)$ for different global rotation rates $\tilde{\Omega}^G$ in the deformed sphere with an eccentricity $\varepsilon = 0.20$ and a fixed fluid rotation $\tilde{\Omega}^F = 0.500 \pm 0.005$ Hz ($Re = 1.49 \times 10^3$). The measured number n of axial half-wavelengths is also indicated. Here, all pictures have been rotated by 90° for convenience.

progressively decreasing the global rotation rate, we have observed that various bands of resonance coexist for $\Omega^G \geqslant \Omega_c^G \sim -1/2$, first separated by large regions of stability (especially for cyclones, i.e. $\Omega^G > 0$), then progressively overlapping (especially for anticyclones, i.e. $\Omega^G < 0$). All resonances sharply disappear once the global rotation rate reaches a critical value $\Omega_c^G \sim -1/2$. Focusing on the stationary modes $(-1, 1, 1)$, we have shown that the instability wavenumber as well as its growth rate significantly increase and reach a maximum just before Ω_c^G. In the cylindrical geometry, all these results agree quantitatively with the theoretical estimations obtained from a mixed theory, where the viscous growth rate determined by a short-wavelength analysis in the limit of small elliptical deformations is expressed in terms of global parameters. Our conclusions for the cylinder and the sphere also agree qualitatively with the general trend observed by Afanasyev (2002) for vortex pairs and by Stegner *et al.* (2005) for Kármán vortex streets, even though our experimental set-up is totally different (i.e. their vortices are not confined and are subjected to rather large elliptical deformations). Both studies report the systematic destruction of elliptical anticyclones by a sinusoidal mode with a decreasing wavelength when Ω^G decreases to a certain critical value, corresponding to the overlapping $(-1, 1, 1)$ resonances mentioned here. We thus argue that this behaviour is universal, except for the explicit value of Ω_c^G that will depend both on the vortical structure considered and on the value of the eccentricity (see also Sipp *et al.* 1999; Le Dizès 2000).

Theory		Experiments			
Ω^G	n	$\tilde{\Omega}^F$ (Hz)	$\tilde{\Omega}^G$ (Hz)	Ω^G	n
0	1	0.500	0	0	1
		0.747	0	0	1
−0.338	2	0.500	−0.141	−0.282	2
		0.500	−0.170	−0.340	2
		0.500	−0.184	−0.368	2
		0.747	−0.232	−0.311	2
		0.747	−0.261	−0.349	2
		0.755	−0.217	−0.287	2
		0.755	−0.242	−0.3205	2
		0.755	−0.250	−0.331	2
		0.755	−0.252	−0.334	2
		0.755	−0.270	−0.358	2
−0.4145	3	0.500	−0.194	−0.388	3
		0.500	−0.196	−0.392	3
		0.500	−0.200	−0.400	3
		0.500	−0.202	−0.404	3
		0.500	−0.210	−0.420	3
		0.747	−0.299	−0.400	3
−0.446	4	0.500	−0.218	−0.436	4
		0.500	−0.226	−0.452	4
		0.747	−0.341	−0.4565	4
		0.755	−0.318	−0.421	4
		0.755	−0.333	−0.441	4
		0.755	−0.346	−0.458	4
−0.473	5	0.500	−0.238	−0.476	5
−0.483	8	0.500	−0.242	−0.484	5
−0.4865	9	0.750	−0.365	−0.487	5
−0.489	10	0.500	−0.266	−0.488	5
−0.500	∞	0.500	−0.250	−0.500	6
		0.747	−0.373	−0.499	5
		0.500	−0.264	−0.528	6
		0.500	−0.269	−0.538	6
		0.500	−0.279	−0.558	7
		0.750	−0.382	−0.509	5
		0.750	−0.383	−0.511	5
		0.750	−0.401	−0.535	5
		0.750	−0.406	−0.541	6
		0.750	−0.408	−0.544	6
		0.747	−0.388	−0.519	5
		0.747	−0.401	−0.537	5
		0.747	−0.409	−0.5475	6

TABLE 3. Measured parameters and theoretical predictions for the instability modes $(-1, 1, 1)$ observed in a sphere of radius $\tilde{R} = 2.175$ cm and eccentricity $\varepsilon = 0.20$. The number n of axial half-wavelengths is measured for various values of $\tilde{\Omega}^G$ and $\tilde{\Omega}^F$. Theoretical results come from the determination of perfect resonances by the global approach. Sketches and experimental pictures of the corresponding mode are shown in figures 10 and 11 respectively.

Conclusions for the spherical geometry are especially interesting in the geophysical and astrophysical contexts. For instance, complex motions can be expected in the Earth's core in addition to the simple spin-over excited by both precession and elliptical instability. More generally, one can imagine that binary stars and moon–planet systems where the elliptical instability is expected to occur, encounter various

bands of instability during their evolution: depending on the relative changes in their rotation and revolution rates, different and complex histories for energy dissipation and flow motions can thus be expected. Clearly, the role of the elliptical instability in natural flows, as suggested for instance by Kerswell & Malkus (1998), still requires more work, in order to fully understand the implications of all natural complexities for the standard and well-known hydrodynamical model (see also Lacaze *et al.* 2006; Le Bars & Le Dizès 2006).

The authors would like to thank David Guimbard for his constructive comments on a earlier version of this paper.

REFERENCES

Afanasyev, Y. D. 2002 Experiments on instability of columnar vortex pairs in rotating fluid. *Geophys. Astrophys. Fluid Dyn.* **96**, 31–48.

Aldridge, K., Seyed-Mahmoud, B., Henderson, G. & van Wijngaarden, W. 1997 Elliptical instability of the Earth's fluid core. *Phys. Earth Planet. Inter.* **103**, 365–374.

Bayly, B. J. 1986 Three-dimensional instability of elliptical flow. *Phys. Rev. Lett.* **57**, 2160–2163.

Boubnov, B. M. 1978 Effect of Coriolis force field on the motion of a fluid inside an ellipsoidal cavity. *Izv. Atmos. Ocean. Phys.* **14**, 501–504.

Craik, A. D. D. 1989 The stability of unbounded two- and three-dimensional flows subject to body forces: some exact solutions. *J. Fluid Mech.* **198**, 275–292.

Craik, A. D. D. & Criminale, W. O. 1986 Evolution of wavelike disturbances in shear flows – a class of exact solutions of the Navier-Stokes equations. *Proc. Roy. Soc. Lond.* A **406**, 13–26.

Eloy, C., Le Gal, P. & Le Dizès, S. 2000 Experimental study of the multipolar vortex instability. *Phys. Rev. Lett.* **85**, 3400–3403.

Eloy, C., Le Gal, P. & Le Dizès, S. 2003 Elliptic and triangular instabilities in rotating cylinders. *J. Fluid Mech.* **476**, 357–388.

Friedlander, S. & Vishik, M. 1991 Instability criteria for steady flows of a perfect fluid. *Phys. Rev. Lett.* **66**, 2204–2206.

Gledzer, E. B. & Ponomarev, V. M. 1992 Instability of bounded flows with elliptical streamlines. *J. Fluid Mech.* **240**, 1–30.

Greenspan, H. P. 1968 *The Theory of Rotating Fluids*. Cambridge University Press.

Kerswell, R. R. 1994 Tidal excitation of hydromagnetic waves and their damping in the Earth. *J. Fluid Mech.* **274**, 219–241.

Kerswell, R. R. 2002 Elliptical instability. *Annu. Rev. Fluid Mech.* **34**, 83–113.

Kerswell, R. R. & Barenghi, C. F. 1995 On the viscous decay rates of inertial waves in a rotating circular cylinder. *J. Fluid Mech.* **285**, 203–214.

Kerswell, R. R. & Malkus, W. V. R. 1998 Tidal instability as the source for Io's magnetic signature. *Geophys. Res. Lett.* **25**, 603–606.

Kudlick, M. 1966 On the transient motions in a contained rotating fluid. PhD thesis, MIT.

Lacaze, L., Herreman, W., Le Bars, M., Le Dizès, S. & Le Gal, P. 2006 Magnetic field induced by elliptical instability in a rotating spheroid. *Geophys. Astrophys. Fluid Dyn.* **100**, 299–317.

Lacaze, L., Le Gal, P. & Le Dizès, S. 2004 Elliptical instability in a rotating spheroid. *J. Fluid Mech.* **505**, 1–22.

Le Bars, M. & Le Dizès, S. 2006 Thermo-elliptical instability in a rotating cylindrical shell. *J. Fluid Mech.* **563**, 189–198.

Leblanc, S. & Cambon, C. 1997 On the three dimensional instabilities of plane flows subjected to Coriolis force. *Phys. Fluids* **9**, 1307–1316.

Leblanc, S. & Cambon, C. 1998 Effects of the Coriolis force on the stability of Stuart vortices. *J. Fluid Mech.* **356**, 353–379.

Lebovitz, N. R. & Zweibel, E. G. 2004 Magnetoelliptic instabilities. *Astrophys. J.* **609**, 301–312 .

Le Dizès, S. 2000 Three-dimensional instability of a multipolar vortex in a rotating flow. *Phys. Fluids* **12**, 2762–2774.

Leweke, T. & Williamson, C. H. K. 1998 Cooperative elliptic instability of a vortex pair. *J. Fluid Mech.* **360**, 85–119.

Lifschitz, A. & Hameiri, E. 1991 Local stability conditions in fluid dynamics. *Phys. Fluids* **3**, 2644–2651.

Lubow, S. H., Pringle, J. E. & Kerswell, R. R. 1993 Tidal instability of accretion disks. *Astrophys. J.* **419**, 758–67.

Malkus, W. V. R. 1989 An experimental study of the global instabilities due to the tidal (elliptical) distortion of a rotating elastic cylinder. *Geophys. Astrophys. Fluid Dyn.* **48**, 123–34.

Moore, D. W. & Saffman, P. G. 1975 The instability of a straight vortex filament in a strain field. *Proc. R. Soc. Lond.* A **346**, 413–425.

Pierrehumbert, R. T. 1986 Universal short-wave instability of two-dimensional eddies in an inviscid fluid. *Phys. Rev. Lett.* **57**, 2157–2159.

Potylitsin, P. & Peltier, W. R. 1999 Three dimensional destabilization of Stuart vortices: the influence of rotation and ellipticity. *J. Fluid Mech.* **387**, 205–226.

Rieutord, M. 2003 Evolution of rotation in binaries: physical processes. *Stellar Rotation, Proc. IAV Symp.* **215**, pp. 394–403.

Sipp, D., Lauga, E. & Jacquin, L. 1999 Vortices in rotating systems: centrifugal, elliptic and hyperbolic type instabilities. *Phys. Fluids* **11**, 3716–3728.

Stegner, A., Pichon, T. & Beunier, M. 2005 Elliptical-inertial instability of rotating Karman streets. *Phys. Fluids* **17**, 066602.

Tsai, C.-Y. & Widnall, S. E. 1976 The stability of short waves on a straight vortex filament in a weak externally imposed strain field. *J. Fluid Mech.* **73**, 721–733.

Vladimirov, V. A., Tarasov, V. & Ribak, L. Y. 1983 Stability of elliptically deformed rotation of an ideal incompressible fluid in a Coriolis force field. *Isv. Atmos. Ocean. Phys.* **19**, 437–442.

Waleffe, F. A. 1990 On the three-dimensional instability of strained vortices. *Phys. Fluids* A **2**, 76–80.